

Perpendicularly Reversed Polarization Sensitivity of Double-faced Photodetection based on Sb_2Se_3 Microbelt

Peng Wan, Mingming Jiang,* Longxing Su, Sihao Xia, Yun Wei, Tong Xu, Yang Liu, Daning Shi, Xiaosheng Fang,* and Caixia Kan*

Low-dimensional polarization-sensitive photodetectors have captured ever-increasing attention due to their unique applications in navigation, optical switching, and communication. However, to date, the study of dimensionality-dependent polarization-sensitive photodetectors has not received much attention. Herein, a double-faced polarization-sensitive photodetector based on an individual high-quality Sb_2Se_3 microbelt is proposed, where both the wide and narrow side facets serve as irradiation targets. Polarization-sensitive measurements reveal the anisotropy in the photocurrents recorded parallel and perpendicular to the long axis of the Sb_2Se_3 microbelt. Strikingly, the single Sb_2Se_3 microbelt photodetector reveals the obvious perpendicular reversal with a 90° angle on polarization sensitivity from the wide surface to the narrow surface. With decreasing inclination angle, the anisotropic ratio varies from 1.18 to 0.87 gradually. Interestingly, the photodetector can lose its polarization sensitivity at a particular inclination angle. Angle-resolved polarized Raman spectroscopy confirms the asymmetry and anisotropic character of the Sb_2Se_3 microbelt. The polarization sensitivity of the Sb_2Se_3 microbelt photodetectors originates from the optical anisotropy induced by the crystal structure anisotropy, rather than one-dimensional geometry morphological anisotropy. The use of an anisotropic Sb_2Se_3 microbelt in double-faced polarization-sensitive photodetection may contribute to new functionality in innovative optoelectronic applications.

1. Introduction


Polarization characteristics provide an additional degree of freedom for light that is essentially unrelated to spectral and intensity images, allowing it to convey more information.^[1,2] Polarization-sensitive photodetectors (PDs) are extremely preferred for efficient optical signal collection and optical noise shielding to improve target recognition and identification operating in a complex environment.^[3] As a result, polarization-sensitive PDs offer additional benefits in applications such as navigation, polarization sensors, infrared imaging, and optical switching.^[4,5] Conventional polarization-sensitive PDs require complicated fabrication procedures and complex structures such as polarizers, lens systems, and detection elements.^[6] Whereas, high cost, large volume, and heavyweight impede the miniaturization and integration for next-generation photoelectric devices.^[7,8] Low-dimensional anisotropic materials with polarization characteristics are considered as promising candidates to overcome these issues owing to their tiny size, rich structures, strong light-matter interactions, and excellent compatibility.^[1,9]

Generally, low-dimensional anisotropic materials as an active layer in constructing polarization-sensitive PDs include 2D and 1D materials. The emerging 2D materials such as black phosphorus, GeSe_2 , ReS_2 , and PdSe_2 greatly boost the detection of polarization light owing to their intrinsic anisotropic crystal structures and high optical sensitivity.^[10–13] Despite their great polarization sensitivity, polarization-sensitive PDs based on anisotropic 2D materials are typically single-faced due to natural dimension restrictions. 1D materials, particularly 1D nano/microstructures, may contain not only inherent anisotropy but also morphological anisotropy in the geometric structure along the long axis.^[6] 1D nanostructures, such as InP , TiS_3 , Sb_2Se_3 , and CsPbI_3 , have been utilized to realize polarization-sensitive photodetection.^[14–17] Indeed, the polarization sensitivity of 1D nanostructures mainly originates from anisotropic morphology, because the diameter is much smaller than that of the optical wavelengths, but the length is considerably larger.^[9] The

P. Wan, M. Jiang, S. Xia, Y. Wei, T. Xu, Y. Liu, D. Shi, C. Kan
College of Physics
MIIT Key Laboratory of Aerospace Information Materials and Physics
Key Laboratory for Intelligent Nano Materials and Devices
Nanjing University of Aeronautics and Astronautics
Nanjing 211106, P. R. China
E-mail: mmjiang@nuaa.edu.cn; cxkan@nuaa.edu.cn

L. Su
School of Microelectronics
Southern University of Science and Technology
Shenzhen 518055, P. R. China

X. Fang
Department of Materials Science
Fudan University
Shanghai 200433, P. R. China
E-mail: xshfang@fudan.edu.cn

 The ORCID identification number(s) for the author(s) of this article can be found under <https://doi.org/10.1002/adfm.202207688>.

DOI: 10.1002/adfm.202207688

polarized photocurrent always achieves its maximum when the polarization direction of incident light is parallel to the long axis of 1D nanostructures.^[6,14,15] The influence of crystal structure anisotropy and multi-faceted features on the polarization-sensitive PDs based on 1D nanostructures will be overshadowed. To date, advancement has been limited to single-faced in-plane polarization-sensitive PDs. Low-dimensional multi-faceted polarization-sensitive PDs have not been examined experimentally yet. However, the discovery of dimensionality-dependent anisotropy and multi-faceted polarization sensitivity is of special scientific and technological importance, which may provide new functionality for optoelectronics in the future.

In this work, 1D antimony selenide microbelts (Sb_2Se_3 MBs) with high-quality and uniform sizes are synthesized via the chemical vapor deposition (CVD) method. Using MXene as symmetric electrodes, the CVD-synthesized Sb_2Se_3 MBs are used to develop photoconductive photodetection devices. The MXene- Sb_2Se_3 -MXene PDs exhibit favorable near-infrared (NIR) photodetection with the maximum photoresponse wavelength located ≈ 1050 nm, and manifest outstanding repeatability and faster photoresponse speed. In particular, the asymmetry and anisotropic character of the Sb_2Se_3 MBs in three axial directions are revealed by angle-resolved polarized Raman spectroscopy, which is well consistent with the theoretical prediction by Raman tensors. Double-faced polarization-sensitive PD based on individual Sb_2Se_3 MB is proposed, in which both the wide and narrow side facets act as irradiation targets. Sb_2Se_3 MB-based polarization-sensitive PD reveals the obvious perpendicular reversal with a 90° angle on polarization sensitivity from the wide irradiation surface to the narrow irradiation surface. The anisotropic ratio decreases gradually from 1.18 to 0.87, as the wide irradiation surface rotates to the narrow irradiation surface. According to finite element method analysis, 1D geometry morphological anisotropy cannot substantially contribute to polarization sensitivity. Based on the density functional theory calculations, the perpendicularly reversed polarization sensitivity of the Sb_2Se_3 MB-based PDs originates from the optical anisotropy induced by the crystal structure anisotropy.

2. Results and Discussions

Sb_2Se_3 , a typical V–VI semiconductor, is a prominent contender for photovoltaic and photodetection applications owing to its suitable bandgap (≈ 1.2 eV), large absorption coefficient ($>10^5$ cm^{-1}), non-toxicity, and abundance on the earth.^[18–22] The Sb_2Se_3 semiconductor belongs to space group $Pbnm$ (62) and has an orthorhombic crystal structure with the lattice constants of $a = 1.162$ nm, $b = 1.177$ nm, and $c = 0.396$ nm.^[23] The crystal structure of Sb_2Se_3 materials consists of zigzag chain-like $(\text{Sb}_4\text{Se}_6)_n$ ribbons connecting along the [001] direction through strong Sb–Se covalent bonds, whereas stacking in the [100] and [010] directions through weak Vander Waals force (See Figure 1a and Figure S1 in Supporting Information).^[24] The interactions between the chains are relatively weaker than the interactions within the chains, indicating that the Sb_2Se_3 crystals exhibit anisotropic properties in all three axial directions.^[25] Further, natural cleavage would take place on (010) planes, with pref-

erential growth occurring in the [001] direction.^[26,27] As we described in Experimental Section, individual Sb_2Se_3 MBs are synthesized through a simple chemical vapor deposition (CVD) method. The schematic diagram of the growth is illustrated in Figure 1b. Briefly, the high-purity powder of Sb and Se serves as the precursor, and argon (Ar) is employed as the carrier gas. The cleaned Si is chosen as the growth substrate, which is placed above the Sb powder with the polished surface facing down.

The length of the as-synthesized Sb_2Se_3 MBs ranges from 0.3 to 1.0 cm and the typical optical image is shown in Figure S2 (Supporting Information). A scanning electron microscope (SEM) image of the individual Sb_2Se_3 MB is shown in Figure 1c. The wide top surface of Sb_2Se_3 is relatively smooth and uniform in comparison with the side surface. The cross-section of the Sb_2Se_3 MB is nearly rectangular, with a width of ≈ 100 μm and a thickness of ≈ 40 μm (Figure S3, Supporting Information). The MB is made up of bundles of whiskers arranged parallel to the MB's long axis, according to a higher magnification image of the MB's edge (Figure S4, Supporting Information). These whiskers are expected to be parallel to the [001] axis of the Sb_2Se_3 MB.^[28] The size distribution of some Sb_2Se_3 MBs is counted in the histogram (Figure S5, Supporting Information). Despite the low width-to-thickness ratio (2–6), the smooth top surface is generally larger than the side surface at the same length. The growth rate r of the nuclei along the a -axis, the b -axis, and the c -axis is in the sequence of $r_c \gg r_a > r_b$.^[29–31] The smooth and wide top surface can be assumed to represent the cleavage plane (010) due to the significant cleavage ability, which is perpendicular to the b -axis. The element distribution and composition of the MB were determined using energy-dispersive X-ray (EDX) mapping and analysis. As shown in Figure 1d, the Sb and Se elements are distributed uniformly throughout the Sb_2Se_3 MB. The atomic proportion of Sb:Se in MB is 39.9:60.1 (Figure S6, Supporting Information), which is consistent with the standard stoichiometric proportion. The elemental composition and the purity of as-prepared Sb_2Se_3 MBs were further confirmed using X-ray photoelectron spectroscopy (XPS). The high-resolution spectra of Sb 4d and Se 3d core levels are shown in Figure S7 (Supporting Information). The fitted curves of Sb 4d peaking at 34.39 and 35.66 eV can be attributed to Sb $4d_{5/2}$ and Sb $4d_{3/2}$, respectively. The fitted curves of Se 3d peaking at 53.92 and 54.95 eV correspond to Se $3d_{5/2}$ and Se $3d_{3/2}$, respectively. These results are consistent with the previously reported literature, indicating that the as-prepared Sb_2Se_3 MBs are phase-pure.^[24,32]

As shown in Figure 1e, the crystal lattice fringes are clearly distinguished in the high-resolution transmission electron microscopy (HRTEM) image of an individual Sb_2Se_3 MB. The measured lattice spacing of 0.294 and 0.330 nm can be assigned to the orthorhombic Sb_2Se_3 crystal lattice's (040) and (021) planes, respectively. The angle formed by the (040) and (021) planes is $\approx 55.6^\circ$, which matches well with the calculated result based on the crystal structure. The experimental finding confirms that the CVD-grown Sb_2Se_3 MBs grow along the [001] direction, which corresponds to c -axis. In addition, the selected area electron diffraction (SAED) pattern can be indexed to orthorhombic Sb_2Se_3 , determining single crystal nature (Figure S8, Supporting Information). Figure 1f shows X-ray diffraction

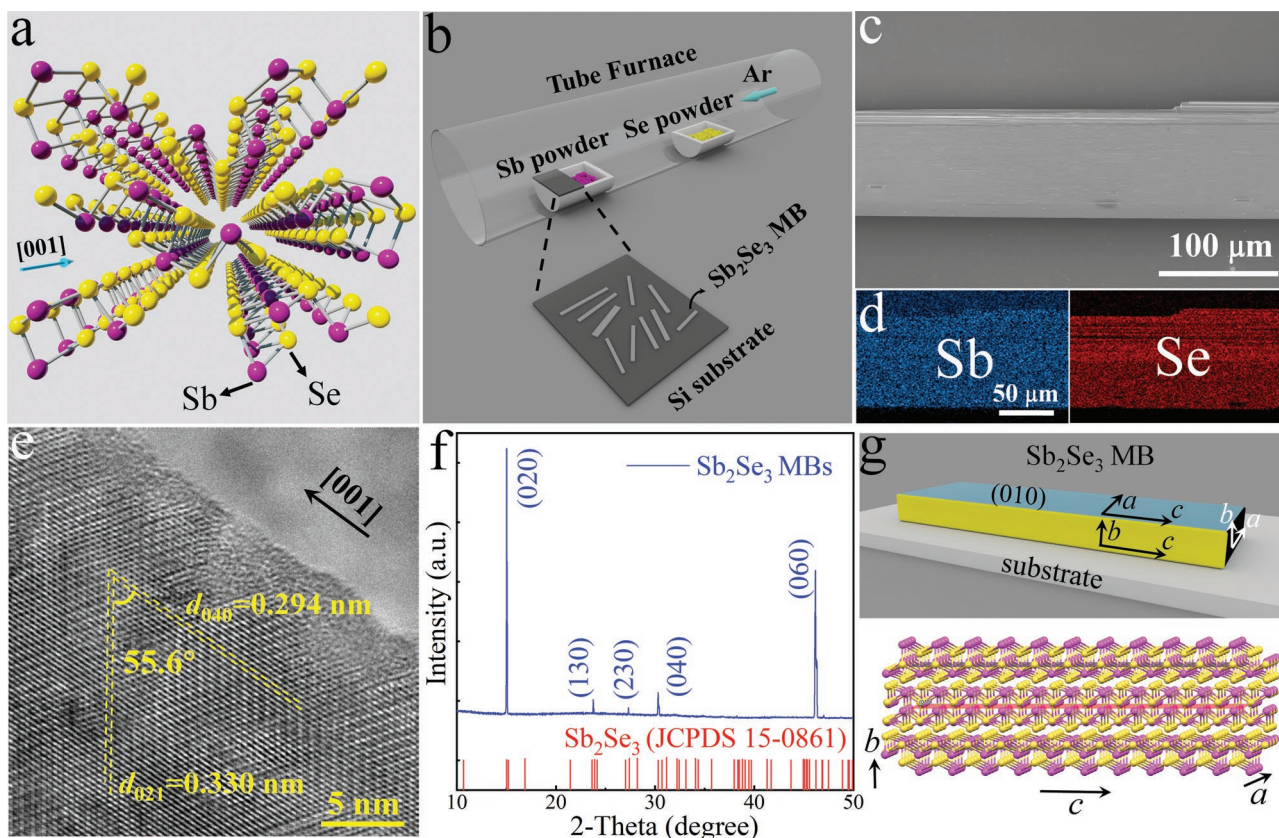


Figure 1. Atomic structure, growth, morphology, and characterizations of the Sb_2Se_3 MBs. a) Atomic model of $(\text{Sb}_4\text{Se}_6)_n$ ribbons viewed along the [001] direction. b) Schematic diagram of the growth of Sb_2Se_3 MBs on Si substrate. c) SEM image of the as-synthesized Sb_2Se_3 MB. d) EDX mapping observation of a single Sb_2Se_3 MB, confirming the uniform distribution of Sb and Se elements. e) HRTEM image of the Sb_2Se_3 MBs. f) XRD pattern of the Sb_2Se_3 MBs. g) Crystallographic a , b , and c -axes of a single Sb_2Se_3 MB. The corresponding 3D atomic model is shown in the bottom panel.

(XRD) patterns of the as-prepared Sb_2Se_3 MBs. All the diffraction peaks can be indexed to the orthorhombic phase of Sb_2Se_3 (JCPDS Files No.15-0861).^[33] Any additional phases, such as Se and Sb_2O_3 , are not detected, demonstrating the high purity of the Sb_2Se_3 MBs.^[34] The patterns exhibit the abnormally strong intensity of those (0k0) peaks of the orthorhombic phase Sb_2Se_3 and other reflection peaks are extremely weak or absent in this pattern. To further explore the orientation of Sb_2Se_3 MBs, the texture coefficient of the (0k0) peaks ($\text{TC}_{(0k0)}$) is calculated in Note S9 (Supporting Information).^[35,36] As shown in Figure S9 (Supporting Information), large TCs for diffraction peaks reveal that the preferred orientation is along [010] direction. The results further validate the aforementioned assumption that the wide top surface is the cleavage plane (010). Because the long axis of the Sb_2Se_3 MB is the c -axis, the crystallographic a , b , and c axes of Sb_2Se_3 MB can be determined (Figure 1g). The wide top surface and narrow side surface are marked as a - c and b - c surfaces, respectively. Furthermore, the $(\text{Sb}_4\text{Se}_6)_n$ ribbon-like structures horizontally stack in parallel with the substrate, as presented in the bottom of Figure 1g.

Unpolarized Raman spectrum used to determine the crystalline structure and vibration mode of the Sb_2Se_3 MB was measured. Considering the photostability of the Sb_2Se_3 ,^[24] the Raman spectra of the Sb_2Se_3 MB were measured using a 532 nm laser with different intensities. As shown in Figure 2a,

the Raman peaks centered at 122, 153, 187, and 211 cm^{-1} originate from the vibration modes of Sb_2Se_3 when the light intensity is below 602 μW .^[28,37,38] As the light intensity increases further, the Raman peaks at 250 cm^{-1} together with 373 and 450 cm^{-1} appear. The phenomenon may be caused by the damage of Sb_2Se_3 MB (Figure S10, Supporting Information). The product of new materials (the oxidation of Sb_2Se_3 into α - Sb_2O_3 in ambient air) under high-intensity laser irradiation could be yielded.^[24,37,38] No obvious Raman characteristic peak of Sb_2O_3 under low-intensity laser irradiation means that the surface oxidation process is very slow at room temperature. It can be attributed to the fact that parallel-stacked ribbons of Sb_2Se_3 substantially provide no dangling bonds, even at grain boundaries.^[35] Furthermore, there is no Raman mode assignment for amorphous Se or trigonal Se secondary phase in the Raman spectra, robustly supporting the excellent crystal quality of the as-prepared Sb_2Se_3 MBs.^[37,38]

The lattice orientation of materials plays a critical role in the photoelectric properties and their application in functional devices.^[39] Angle-resolved polarized Raman spectroscopy (ARPRS), which has been widely employed in anisotropic two-dimensional materials,^[32,40] was used to investigate the crystal orientation and anisotropic behavior of Sb_2Se_3 MBs. Both the a - c and b - c surfaces of Sb_2Se_3 MBs were examined using the ARPRS. The detailed test method is described in Note S11

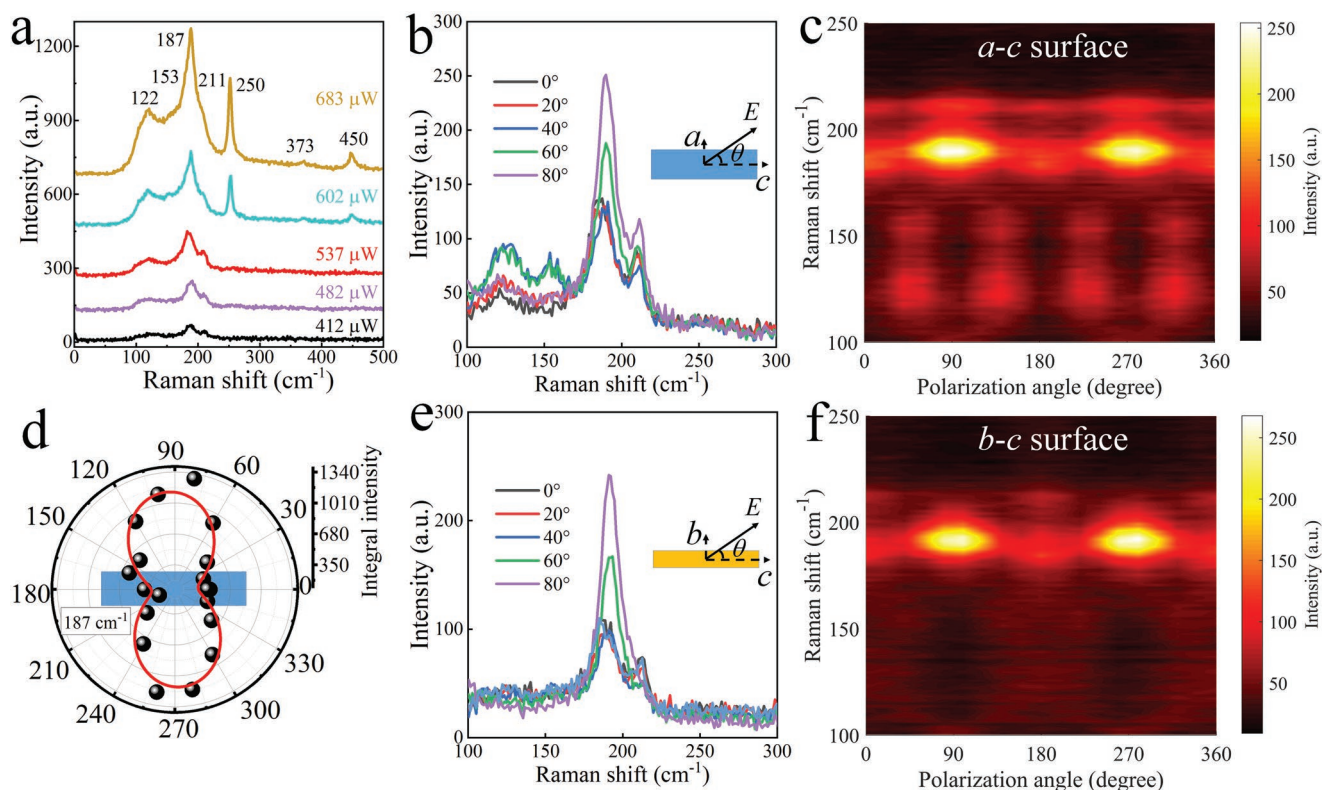


Figure 2. Unpolarized Raman spectra and angle-resolved polarized Raman spectra of the Sb_2Se_3 samples. a) Unpolarized Raman spectra of a Sb_2Se_3 MB measured at 532 nm laser irradiation with different intensities. b) Angle-resolved polarized Raman spectra of the Sb_2Se_3 MB as functions of the polarization angle (θ), in which the irradiation surface is a - c surface. Inset: the θ is the angle between the polarization vector and the c -axis in the a - c surface. c) The corresponding 2D mapping of Raman spectra with respect to the θ (a - c surface). d) Polar plots for the integrated Raman intensity of 187 cm^{-1} peak with respect to the θ . e) Angle-resolved polarized Raman spectra of the Sb_2Se_3 MB as functions of the θ , where the irradiation surface is b - c surface. Inset: the θ is the angle between the polarization vector and the c -axis in the b - c surface. f) The corresponding 2D mapping of Raman spectra with respect to the θ (b - c surface).

(Supporting Information). As shown in Figure 2b, the Raman peaks for the a - c surface of the Sb_2Se_3 MBs show various trends with increasing polarization angles. More specifically, the Raman peaks at 187 and 211 cm^{-1} exhibit a periodicity of 180° and have minimum (maximum) intensity at $\theta = 0^\circ$ ($\theta = 90^\circ$). The Raman peaks at 122 and 153 cm^{-1} have minimum (maximum) intensity at $\theta = 0^\circ$ ($\theta = 45^\circ$) with a periodicity of 90° (Figure 2c). These results can also be clearly observed from the polar plots for the Raman integral intensity of each peak (Figure 2d and Figure S12, Supporting Information). For b - c surface of the Sb_2Se_3 MBs, the peaks at 187 and 211 cm^{-1} follow a similar pattern with a periodicity of 180°, whereas the peaks at 122 and 153 cm^{-1} completely disappear (Figure 2e,f).

To probe these obtained results, the angle-dependent intensities of the Raman active modes are analyzed through the Raman tensor.^[5] The intensity of Raman scattering light (I) is described as

$$I \propto |\vec{e}_i \bar{R} \vec{e}_s|^2 \quad (1)$$

where \bar{R} is Raman tensor. The \vec{e}_i and \vec{e}_s are the polarization vectors of the incident and scattered light, respectively. Combined with the crystal planes of the Sb_2Se_3 MB and the Raman tensor elements of the D_{2h} point group,^[41] the relations between the

intensities of Raman active modes and the polarization angle (θ) are expressed as

$$I_{a-c}^{A_g} \propto (A \sin^2 \theta + C \cos^2 \theta)^2 \quad (2)$$

$$I_{a-c}^{B_{2g}} \propto (E \sin 2\theta)^2 \quad (3)$$

$$I_{b-c}^{A_g} \propto (C \sin^2 \theta + B \cos^2 \theta)^2 \quad (4)$$

$$I_{b-c}^{B_{2g}} = 0 \quad (5)$$

where the $I_{a-c}^{A_g}$ and $I_{a-c}^{B_{2g}}$ are the intensities of Raman A_g and B_{2g} modes for a - c surface of the Sb_2Se_3 MB, respectively. The $I_{b-c}^{A_g}$ and $I_{b-c}^{B_{2g}}$ are the intensities of Raman A_g and B_{2g} modes for b - c surface, respectively. The A , B , C , and E are the elements of the Raman tensor. The detailed derivation is given in Note S13 (Supporting Information).

Given the crystal plane and the symmetries of Raman peaks, the angle-dependent intensity of Raman peaks can be identified. The Raman peaks at 187 and 211 cm^{-1} correspond to A_g vibration mode of Sb_2Se_3 , whereas the Raman peaks at 122 and 153 cm^{-1} are associated with B_{2g} vibration mode of Sb_2Se_3 .^[28,38] Thus, the intensities of Raman peaks at 187 and 211 cm^{-1} in a - c and b - c surfaces have a periodicity of 180° (Figure 2c,f), which agrees well with Equations 2 and 4. According to Equation 3,

the intensities of Raman peaks at 122 and 153 cm^{-1} in *a-c* surface repeat after 90° due to their dependence on 2θ . The Raman peaks at 122 and 153 cm^{-1} in *b-c* surface will disappear based on Equation 5. We further measure the angle-resolved polarized Raman spectroscopy when the oxidation of Sb_2Se_3 into Sb_2O_3 under high-intensity laser irradiation is yielded. As shown in Figure S13 (Supporting information), the Raman intensity shows no dependence on the polarization angle when the Sb_2Se_3 is oxidized into Sb_2O_3 . It demonstrates that the polarization sensitivity of the Sb_2Se_3 MB-based PDs, which will be discussed later, originates from the structural anisotropy of the Sb_2Se_3 MB, rather than the oxidation of Sb_2Se_3 . Briefly, Raman spectroscopy signals are highly sensitive to crystal orientation due to selection rules. The experimental results are perfectly consistent with the Raman intensities calculated based on the crystal structure of Sb_2Se_3 MB, further verifying the crystal direction and strong structural anisotropy of as-grown samples. The structural anisotropy is always directly relevant to the optical and electrical anisotropy, indicating that the as-prepared Sb_2Se_3 MBs offer a great opportunity to exploit it in novel and multi-functional optoelectronic devices.

To further explore the potential applications in optoelectronic devices, a photodetection device made of a single Sb_2Se_3 MB was fabricated. In the device, MXene was used as symmetric electrodes (Experimental Section for more details). The Raman spectra and XRD patterns of MXene confirm the successful synthesis of the few-layered MXene (Figure S14, Supporting information). The schematic diagram of the as-fabricated device and the corresponding optical microscope photograph are shown in Figure 3a. Figure 3b depicts the *I-V* characteristic curves of the Sb_2Se_3 MB-based PD under dark and light illumination with wavelengths ranging from 400 to 1100 nm. An obvious photoresponse is achieved under various light illuminations, implying that the Sb_2Se_3 MB-based PD has the ability to detect light from the ultraviolet to NIR range. Responsivity ($R(\lambda)$), representing the photoelectric conversion capability of a PD, is calculated as^[42]

$$R(\lambda) = (I_{\text{ph}} - I_{\text{d}}) / PS \quad (6)$$

where I_{ph} , I_{d} , P , and S are the photocurrent, the dark current, the light power density, and the effective illumination area ($\approx 3 \times 10^{-3} \text{ cm}^2$), respectively. As displayed in Figure 3c, the spectral responsivity varying from 300 to 1200 nm was acquired under different biases. It can be found that the responsivity in the NIR region is remarkably larger than that in UV or visible regions, which is attributed to the narrow bandgap of Sb_2Se_3 .^[21] In addition, the specific detectivity reaches a maximum at the wavelength of 1050 nm (Figure S15, Supporting information), which means that the weak light signal in the NIR region can be detected by the Sb_2Se_3 -based PDs. As shown in Figure 3d, the *I-t* characteristic curves of the Sb_2Se_3 MB-based PD are measured under 940 nm light with different power densities at 10 V bias. The photocurrent behavior is well maintained as the number of on-off switching cycles increases, suggesting exceptional stability and reproducibility of the Sb_2Se_3 MB-based PDs. In addition, higher photoresponse is observed under the higher light power density due to the enhancement of photo-induced carriers. Accordingly, the light power inten-

sity-dependent photocurrent and responsivity are displayed in Figure 3e. The photocurrent (I) can be described by a simple power law: $I \propto P^\alpha$.^[43] The α is calculated to be 0.32, indicating a complex process of electron-hole generation, recombination, and trapping in the Sb_2Se_3 MB-based PD.^[44]

The response time of the Sb_2Se_3 MB-based PD is measured in Figure 3f. From the figure, the rise time (τ_{rise}) and fast decay time (τ_{decay1}) are estimated to be ≈ 144 and ≈ 96 ms, respectively, which is comparable to or even better than the previously reported results.^[18,44,45] Additionally, the long decay time (τ_{decay2}) is estimated to be 5.52 s, which can be attributed to carrier trapping-releasing from defects.^[46] To further verify the operating mechanism of the Sb_2Se_3 MB-based PD, the positions of energy bands of MXene and Sb_2Se_3 relative to the vacuum level (E_{vac}) are shown in Figure 3g. According to previous literature,^[47,48] the work function of MXene is extracted to be ≈ 5.1 eV; while the conduction band (E_{c}), valence band (E_{v}) and Fermi level (E_{F}) of Sb_2Se_3 are ≈ 4.15 , ≈ 5.35 and ≈ 4.75 eV, respectively. When the Sb_2Se_3 MB contacts the MXene electrode, electrons flow from the Sb_2Se_3 side into the MXene side to achieve thermal equilibrium due to the high E_{F} level of Sb_2Se_3 . A space charge region and built-in electric field will be formed at the interface between the Sb_2Se_3 MB and the MXene. As displayed in the top panel of Figure 3h, the built-in electric field makes the energy band of the Sb_2Se_3 bend at the interface, then forming a potential barrier of 0.55 eV. The potential barrier between the metal and the semiconductor may be lower if the surface states on the side facets of low-dimensional semiconductors are taken into account.^[49,50] Thus, the *I-V* characteristic curve illustrated in Figure 3b (black solid line) shows that the MXene/ Sb_2Se_3 interface approximates an ohmic contact. When the PD is operated under NIR light illumination, the band diagrams are depicted in the bottom panel of Figure 3h. As the Sb_2Se_3 MB is illuminated by the NIR light, the photo-induced generation of electron holes can occur. The carriers, especially the majority carrier (holes), can readily move across the barrier to form photocurrent when the bias is applied.

The intrinsic anisotropy and photoresponse properties of the Sb_2Se_3 MB, as discussed before, allow us to investigate the polarization sensitivity of the Sb_2Se_3 MB-based PD further. Polarization-resolved photocurrents of the Sb_2Se_3 MB-based PD were measured with a NIR light (the central wavelength is 940 nm) serving as the excitation light source. The experimental setup is depicted schematically in Figure 4a. The incident direction of the light source is always perpendicular to the *z-y* plane. The θ is the polarization angle between the polarization direction and the γ -direction (the long axis of the Sb_2Se_3 MB). The substrate can rotate around the γ -axis, and α is the inclination angle between the substrate and the direction of light propagation.

When $\alpha = 90^\circ$, the light beam impinges perpendicularly upon the *a-c* surface of a Sb_2Se_3 MB. As shown in Figure 4b, the obtained photocurrent obviously depends on the polarization angle, where the incident power intensity remains constant. To illustrate the polarization sensitivity of the Sb_2Se_3 MB-based PD intuitively, the polar plots of the polarized photocurrent are displayed in Figure 4c. As the θ rotates from 0° to 360°, the photocurrent exhibits a periodicity of 180°. The photocurrent reaches the maximum when the polarization direction is parallel to the

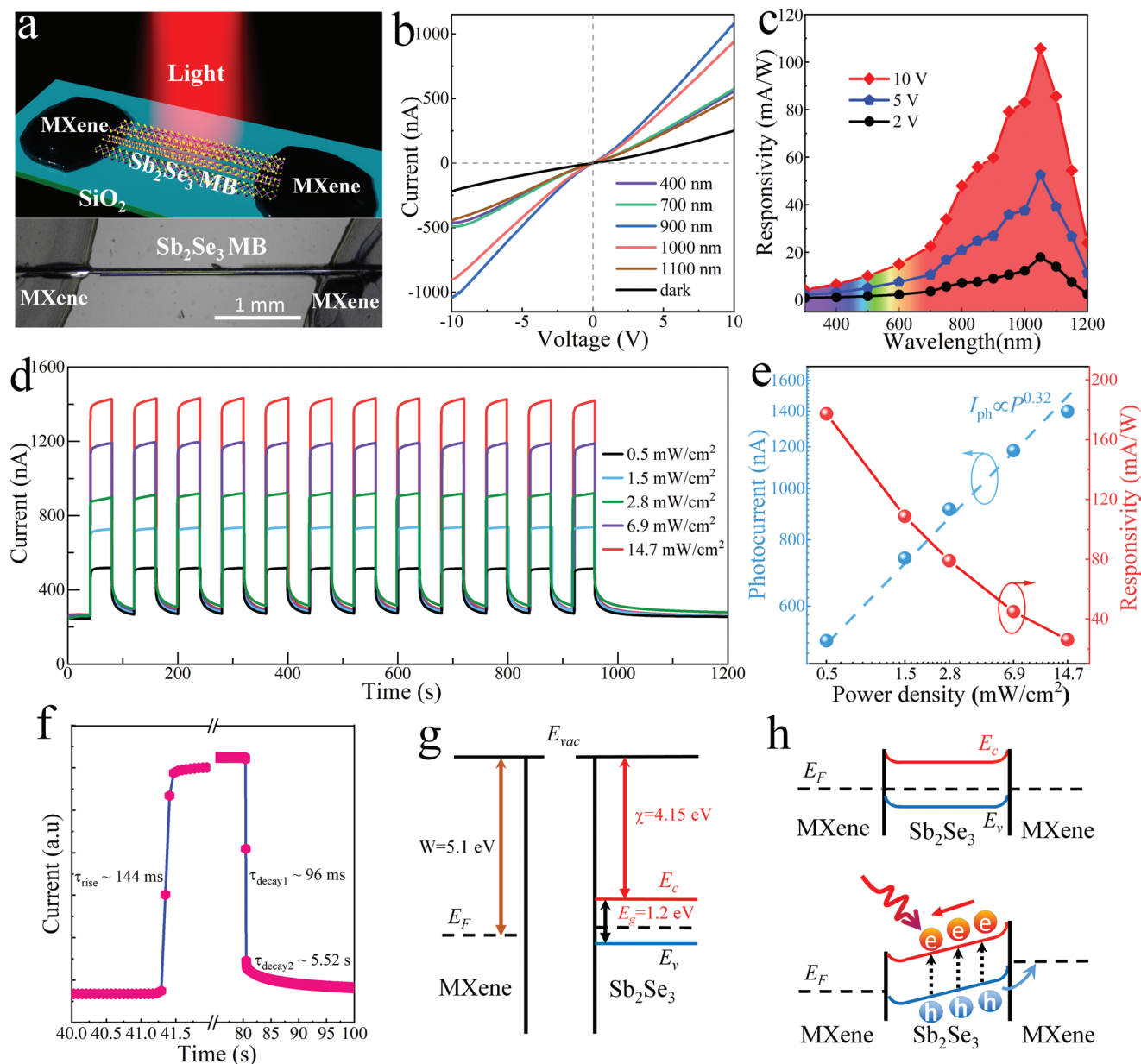


Figure 3. Optoelectronic characteristics of the designed single Sb_2Se_3 MB-based PD. a) Schematic view of the Sb_2Se_3 MB-based PD device structure. The bottom panel is the corresponding optical microscope photograph of the PD. b) I - V characteristic curves of the PD measured under the dark and light illumination with the different wavelengths. c) Wavelength-dependent responsivity of the PD. d) I - t characteristic curves of the PD measured under the 940 nm light illumination with the power density ranging from 0.5 to 14.7 mW cm^{-2} . e) Light power density-dependent photocurrent and responsivity of the PD. f) Time-resolved photoresponse of the PD. g) The positions of the energy band of MXene and Sb_2Se_3 . h) Energy band diagrams of the PD (the upper panel) and carriers' hopping under NIR light with the electrode biased (the bottom panel).

long axis of the Sb_2Se_3 MB. When the polarization direction is perpendicular to the long axis, the photocurrent reaches its minimal value. These points were fitted by the following function:^[39]

$$I_{\text{ph}}(\theta) = I_{\parallel} \cos^2 \theta + I_{\perp} \sin^2 \theta \quad (7)$$

where the I_{\parallel} and I_{\perp} represent the photocurrents when the polarization direction is parallel and perpendicular to the long axis, respectively. The polarized photocurrent is further measured under light illumination with various power densities at

different voltages (Figure 4d). It can be found that the Sb_2Se_3 MB-based PD exhibits polarization sensitivity at various voltages. With the power density increasing, the difference between I_{\parallel} and I_{\perp} increases. To further evaluate the polarization sensitivity, the anisotropy ratio ρ is defined as^[15]

$$\rho = I_{\parallel}/I_{\perp} = I_{\text{ph}}(0^\circ)/I_{\text{ph}}(90^\circ) \quad (8)$$

As shown in Figure 4e, the anisotropy ratio has a positive relationship with the power density, although it is nearly unaffected

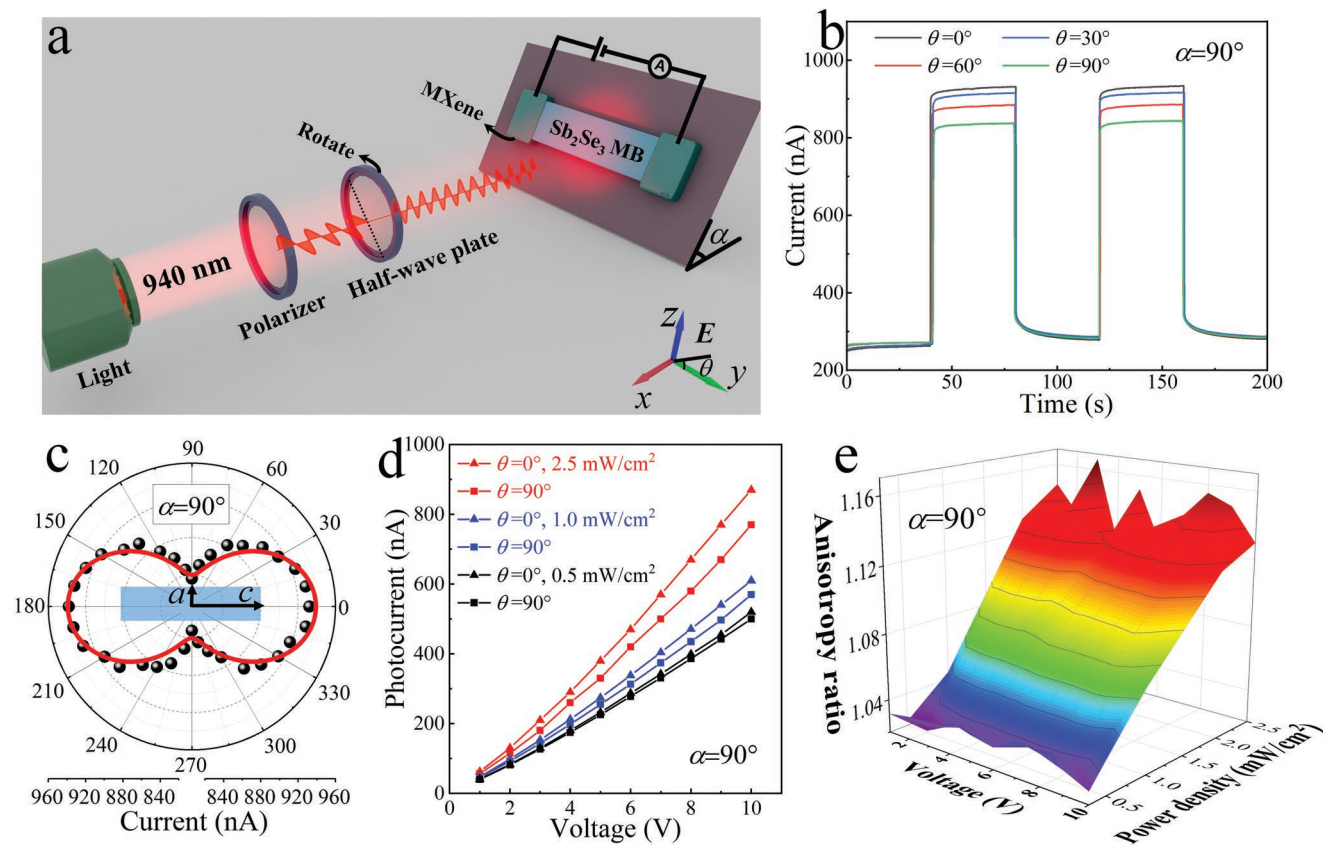


Figure 4. Polarization sensitivity of the Sb_2Se_3 MB-based PD. a) Schematic diagram of the experimental setup for polarization-resolved photocurrent measurement. The substrate is always parallel to the a - c surface of the Sb_2Se_3 MB. b) I - t characteristic curves of the PD measured under the 940 nm light illumination with the polarization angle θ ranging from 0° to 90° ($\alpha = 90^\circ$). c) Corresponding polar plots of the polarized photocurrent. d) The polarized photocurrent at $\theta = 0^\circ$ and $\theta = 90^\circ$ as functions of the biased voltages and the power density of the incident light ($\alpha = 90^\circ$). e) Three-dimensional mapping of the anisotropic ratio as function of the biased voltages and the power density of the incident light ($\alpha = 90^\circ$).

by voltages between 1 and 10 V. It is indicated that the polarization sensitivity cannot originate from the anisotropic electron transport of Sb_2Se_3 .^[32,51] Indeed, since the MXene electrodes are applied on both ends of the Sb_2Se_3 MB, the photo-generated carriers are only transported along the long axis efficiently.

To fully probe the polarization sensitivity of the Sb_2Se_3 MB-based PD, the polarized photocurrent was measured at different inclination angles α . As shown in Figure 5a, I - t characteristic curves show that the polarization photoresponse has a periodicity of 180° . Interestingly, compared with $\alpha = 90^\circ$, the phase lag of polarization photoresponse seems to be 90° when $\alpha = 0^\circ$. Furthermore, the polarization response at $\alpha = 30^\circ$ is significantly weaker than at other inclination angles. The polarization response is explicitly observed in photocurrent graphs when the polarization angle is manually rotated by 20° every 10 s (Figure 5b). Full test cycles are displayed in Figure S16 (Supporting Information). The results are well consistent with Figure 5a, confirming the reliability and reproducibility of polarization sensitivity at different α . For clarity, the corresponding polar plots of the polarized photocurrent at different α are shown in Figure 5c. For $\alpha = 90^\circ$ (a - c surface), the photocurrent reaches the maximum (minimum) when the polarization direction is parallel (perpendicular) to the long axis of Sb_2Se_3 MB. However, the polarization sensitivity of

the Sb_2Se_3 MB-based is perpendicularly reversed for $\alpha = 0^\circ$ (b - c surface). The photocurrent achieves the minimum (maximum) when the polarization direction is parallel (perpendicular) to the long axis of Sb_2Se_3 MB. The b - c surface rotates 90° around the x -axis and the light beam impinges perpendicularly upon the b - c surface of the Sb_2Se_3 MB (Figure S17a, Supporting Information). The polarization photoresponse (Figure S17c, Supporting Information) is consistent with Figure 5, further evidently supporting the perpendicular reversal from the wide surface to the narrow surface. Generally, the oblique incidence of a polarized light source causes a variation in reflectance, which may give rise to absorption and photocurrent differences. To rule out the possibility that the perpendicularly reversed polarization sensitivity is caused by oblique incidence, the substrate is rotated by 90° around the x -axis (Figure S18a, Supporting Information). During tilting of the substrate, the light irradiated on b - c surface is always eliminated. As expected, the perpendicularly reversed polarization sensitivity did not happen with different inclination angles α (Figure S18, Supporting Information).

Considering the different radiation surfaces of Sb_2Se_3 MB with the variation of α , the compromise between polarized photocurrent from a - c surface and b - c surface will appear. Assuming that the incident light energy is totally converted into

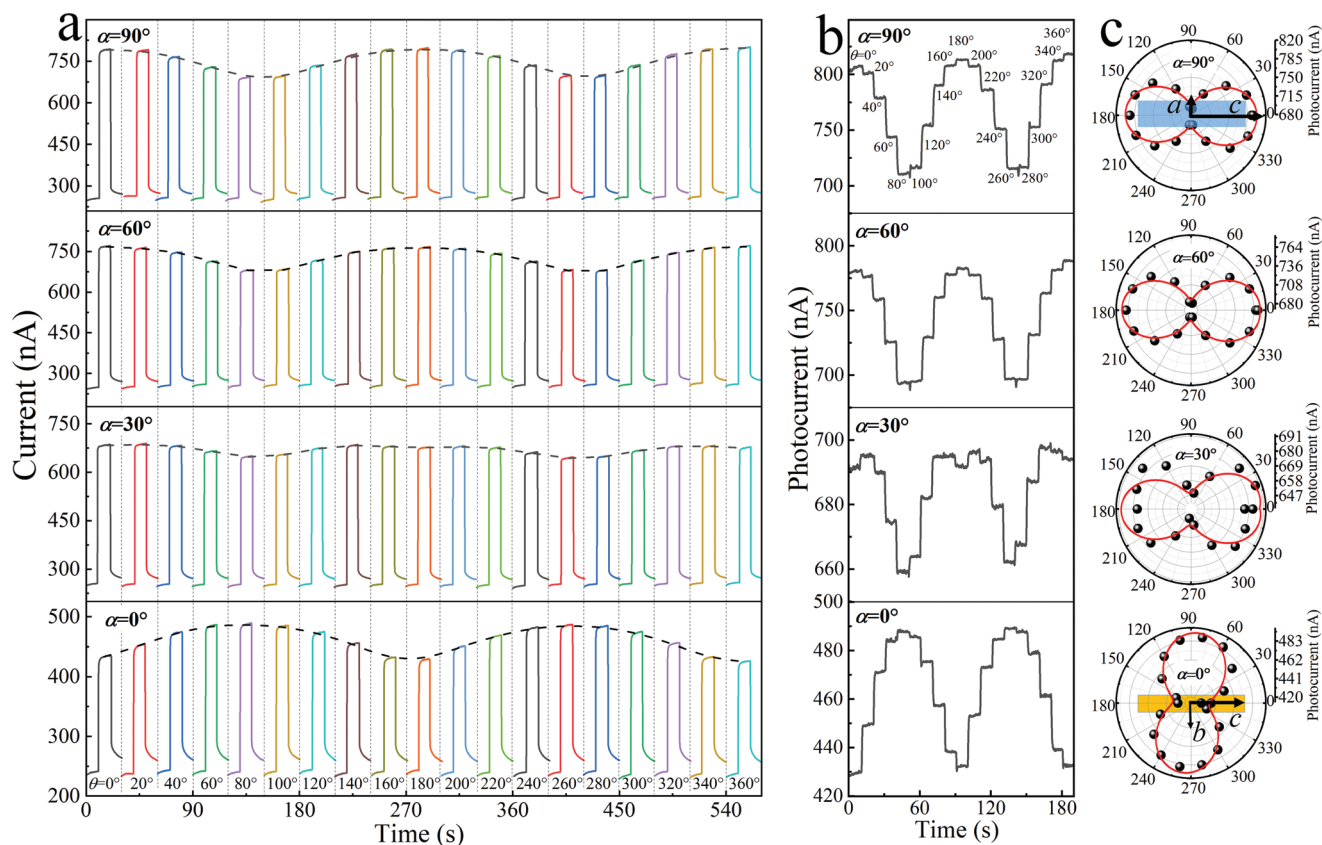


Figure 5. Polarization sensitivity of the Sb_2Se_3 MB-based PD at different inclination angles α . a) I - t characteristic curves of the PD at different α measured under the light illumination with the polarization angle ranging from 0° to 360° . b) The photocurrent of the PD at different α , where the polarization angle is manually rotated by 20° every 10 s. c) Corresponding polar plots of the polarized photocurrent of the PD at different α .

photocurrent, the anisotropy ratio ρ as a function of α can be fitted by the following function:

$$\rho = (I_{\parallel}^{a-c} \sin \alpha + I_{\parallel}^{b-c} \cos \alpha) / (I_{\perp}^{a-c} \sin \alpha + I_{\perp}^{b-c} \cos \alpha) \quad (9)$$

where I_{\parallel}^{a-c} and I_{\perp}^{a-c} are the photocurrent for a - c surface when polarization direction is parallel and perpendicular to the long axis, respectively. I_{\parallel}^{b-c} and I_{\perp}^{b-c} are the photocurrent for b - c surface when polarization direction is parallel and perpendicular to the long axis, respectively. The detailed calculation of fitting function is available in Note S20 (Supporting Information). According to Equation 9, the fitting of the anisotropy ratio as a function of α is shown in Figure 6a. The fitting results slightly deviate from those obtained in the experiments. The cross-section of Sb_2Se_3 MB is not strictly rectangular, which can be one cause of the deviation.

In addition, during the variation of α , the reflectivity of Sb_2Se_3 MB and the photo-generated carrier will also change, further influencing the final polarized photocurrent. Interestingly, it is reasonable to expect that the Sb_2Se_3 MB-based PD will lose its polarization sensitivity at a particular α . Six different Sb_2Se_3 MB-based PDs were fabricated and tested, as illustrated in Figure 6b. The polarization sensitivity of various Sb_2Se_3 MB-based PDs is perpendicularly reversed when $\alpha = 90^\circ$ is turned into $\alpha = 0^\circ$, giving additional confirmation that the above results are universal and repeatable.

To investigate the mechanism of the polarization sensitivity, 1D morphological anisotropy of Sb_2Se_3 MB was first considered. According to the previous research,^[14,52] classical electromagnetic theory can account well for the polarization anisotropy in 1D nanowires. The field distribution of 1D Sb_2Se_3 nano/microstructures is analyzed by finite element method (FEM), in which the polarization of incident light is perpendicular (parallel) to long axis (Note S21, Supporting Information). The polarization anisotropy can not be substantially attributed to the 1D morphological anisotropy of Sb_2Se_3 MB when the cross-sectional size is much larger than that of the optical wavelength of the incident light. Furthermore, the electronic band structure of Sb_2Se_3 is calculated to explore crystal structure anisotropy using first-principle computation based on density functional theory (Figure 6c). The bandgap of Sb_2Se_3 is estimated to be ≈ 1.12 eV, which is consistent with actual bandgap. Generally, the anisotropy of optical properties can play an important role in the polarization sensitivity of photodetection. The dielectric function is a critical parameter that describes optical characteristics. Based on the definition of direct transition probability and Kramers-Kronig dispersion relation, the dielectric function $\epsilon(\omega)$ containing two parts, $\epsilon(\omega) = \epsilon_1(\omega) + \epsilon_2(\omega)i$, can be simulated (Note S22, Supporting Information). The calculated real and imaginary dielectric functions of Sb_2Se_3 along a , b , and c directions are plotted in Figure 6d,e, respectively. A noticeable

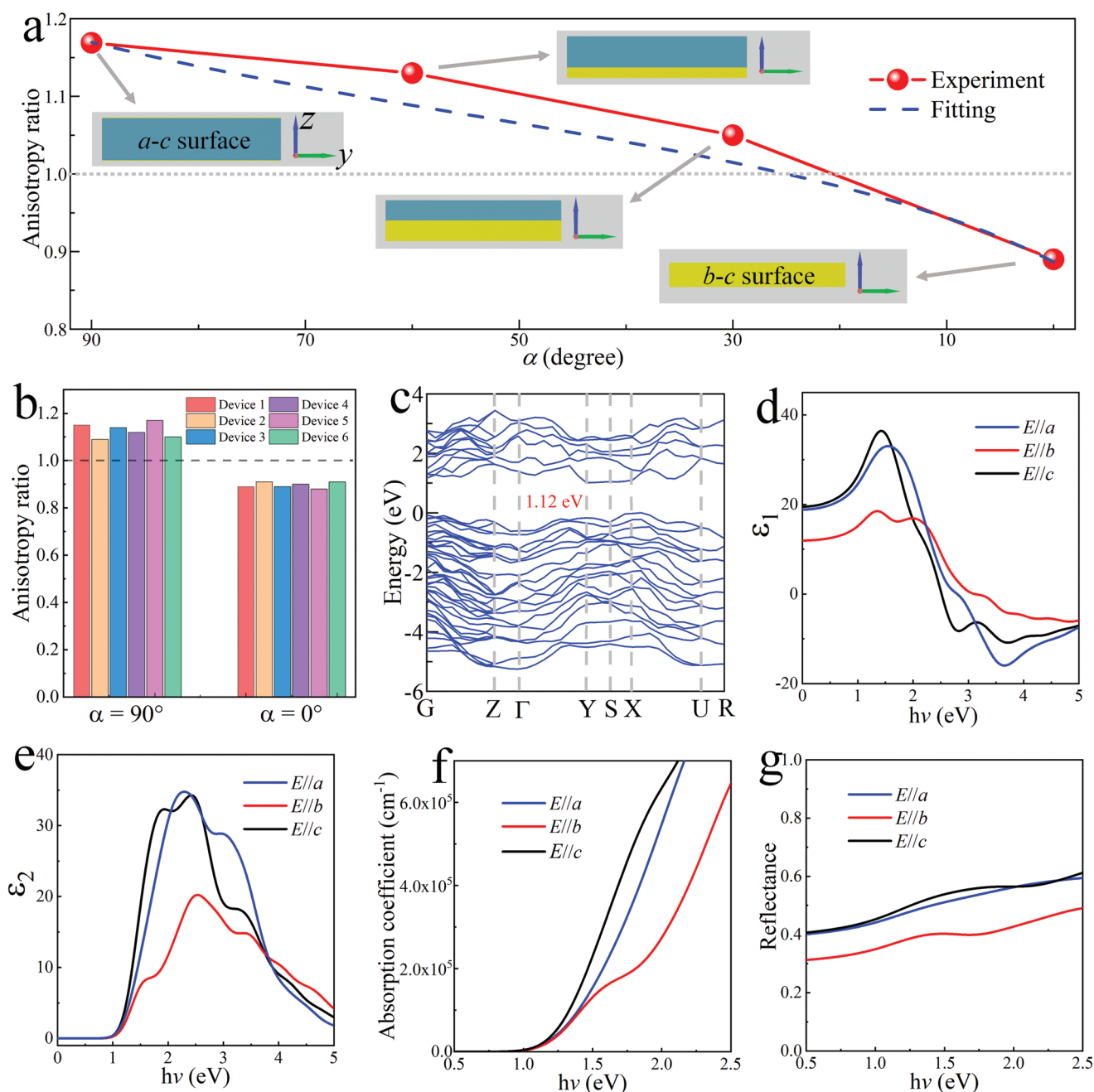


Figure 6. Anisotropic ratio, electronic band structure, and linear dichroism. a) Anisotropic ratio ρ as a function of α . The red dots are experimentally observed data, while the blue dotted line is fitted based on Equation 9. The inset is the radiation surfaces of Sb_2Se_3 MB viewed along the x -axis, corresponding to the red dot. b) Anisotropic ratio ρ at $\alpha = 90^\circ$ and $\alpha = 0^\circ$ for six different Sb_2Se_3 MB-based PDs. c) The calculated electronic band structures of Sb_2Se_3 on the basis of density functional theory. d) The real part of the complex dielectric constant (ϵ_1) of Sb_2Se_3 . e) The imaginary part of the complex dielectric constant (ϵ_2) of Sb_2Se_3 . f) The calculated absorption coefficient (α_{ac}) of Sb_2Se_3 . g) The calculated reflectivity (R) of Sb_2Se_3 .

anisotropic characteristic of Sb_2Se_3 can be proven due to different dielectric responses in various directions.

The absorption coefficient (α_{ac}) and reflectivity (R) of Sb_2Se_3 are obtained by computing the dielectric constant:

$$\alpha_{ac} = \frac{\omega}{c} \sqrt{2(\sqrt{\epsilon_1^2(\omega) + \epsilon_2^2(\omega)} - \epsilon_1(\omega))} \quad (10)$$

$$R = \frac{|\sqrt{\epsilon(\omega)} - 1|^2}{|\sqrt{\epsilon(\omega)} + 1|^2} \quad (11)$$

where ω and c are the angular frequency and the speed of light. As shown in Figure 6f, the absorption coefficient with incident light polarization parallel to the c -axis ($E//c$) is larger than the

absorption coefficient with $E//a$ and $E//b$. This could mean that the polarized photocurrent is always large when the polarization direction is parallel to the c -axis (long axis). However, according to the absorption coefficient ($\approx 10^5 \text{ cm}^{-1}$) for the incident photon energy of 1.32 eV ($\lambda = 940 \text{ nm}$), the penetration depth is calculated to be $\approx 100 \text{ nm}$. The penetration depth is far smaller than the thickness of Sb_2Se_3 MB, which indicates that the transmission light ($\lambda = 940 \text{ nm}$) can be completely absorbed by Sb_2Se_3 MB. It agrees well with the transmission spectrum carried out on Sb_2Se_3 MB (Figure S22, Supporting Information). Thus, the difference between absorption coefficients may not contribute to the polarization sensitivity substantially.

As shown in Figure 6g, the curve of calculated reflectivity ($E//c$) overlaps with the curve of reflectivity ($E//a$). In fact, the measured reflectivity ($E//c$) is smaller than the reflectivity ($E//a$) for the incident photon energy of 1.32 eV in previous literature.^[53] It indicates that more photons will be absorbed to generate the photocurrent when the polarization direction is along the c -axis for a - c surface of Sb_2Se_3 MB. The photocurrent reaches the maximum when the polarization direction is parallel to the long axis for the a - c surface. When polarization direction is along the b -axis, the reflectivity is far smaller than that in the $E//c$ condition. Thus, the photocurrent reaches the maximum when the polarization direction is perpendicular to the long axis for the b - c surface, giving rise to the perpendicularly reversed polarization sensitivity.

3. Conclusion

In summary, double-faced polarization-sensitive PDs based on individual Sb_2Se_3 MB are proposed, in which both the wide and narrow side facets act as irradiation targets. Polarization-sensitive measurements demonstrate anisotropy in the photocurrents recorded on both surfaces. Particularly, the perpendicular reversal with a 90° angle on polarization sensitivity can be observed from the wide irradiation surface to the narrow irradiation surface. The anisotropic ratio decreases from 1.18 to 0.87 gradually with the decrease of inclination angle. The anisotropy rooted in the puckered low symmetry structure of Sb_2Se_3 enables different dielectric responses in various directions. The polarization sensitivity of the Sb_2Se_3 MB-based PDs results from optical anisotropy rather than 1D morphological anisotropy. These results imply that the 1D micro-crystal with intrinsic anisotropy provides another new degree of freedom for fabricating unique multi-functional polarization-sensitive photoelectric devices.

4. Experimental Section

Materials Preparation and Device Fabrication: The growth of Sb_2Se_3 MBs was carried out in a single temperature-zone tube furnace via a simple chemical vapor deposition (CVD) method. In general, the precursor Sb powder (Aladdin, purity 99.99%) was put into a corundum boat where a small piece of Si substrate was put over it and then placed in the central zone of the furnace. The Se powder (Aladdin, purity 99.99%) was put into another corundum boat. Subsequently, it was placed at upstream of the Sb powder. The weight ratio of Se to Sb was 3 to 2. The distance between the two precursors was $\approx 10 \text{ cm}$.

During the reaction process, the growth temperature was maintained at 600°C . 150 sccm Ar gas (99.999%) was utilized as the protective and carrier gas. After the growth process, the tube furnace was cooled down naturally. As a result, Sb_2Se_3 MBs were synthesized on the Si substrate. The as-obtained individual Sb_2Se_3 MB was singled out and transferred onto a quartz substrate. Both ends of Sb_2Se_3 MB were immersed into the few-layered $\text{Ti}_3\text{C}_2\text{T}_x$ colloidal aqueous solution (5 mg mL^{-1} , Nanjing MKNANO Tech. Co., Ltd.) for 1 h. Thus, the Sb_2Se_3 MB-based PDs were fabricated, in which $\text{Ti}_3\text{C}_2\text{T}_x$ (MXene) acted as electrodes.

Characterization and Measurements: The morphology, size, and thickness of Sb_2Se_3 MBs were characterized by a scanning electron microscope (SEM) and an optical microscope (OM). The composition was obtained by an energy dispersive X-ray spectroscopy (EDX) associated with the SEM. The X-ray diffraction (XRD) patterns of the Sb_2Se_3 MBs were measured by an X-ray diffractometer (Cu $K\alpha$ radiation, $\lambda = 0.15406 \text{ nm}$). The Raman spectra were acquired by a microscope-based Raman spectrometer where a 532 nm laser acted as the excitation light. Angle-resolved polarization Raman spectra were obtained by adjusting the polarization angle of the excitation laser with a rotatable half-wave plate. Transmittance spectra were gained by UV-NIR micro-absorption spectrum system (MStarter ABS). The photoelectric properties of the MXene- Sb_2Se_3 -MXene were characterized by a photoelectric test system containing a laser-driven light source (EQ-99X), a monochromator, a chopper, and a semiconductor analysis device (Keysight B1500A). The intensity of incident light was calibrated by a power meter (Vega, Ophir) equipped with a thermal sensor (3A, Ophir). The polarization test system consists of a near-infrared LED emitting light (emitting wavelength is centered at 940 nm), a collimating lens, a linear polarizer, a rotatable achromatic half-wave plate, and a 3D mobile platform where the PDs can be fixed at different angles.

Calculation Methods: The first principle calculation based on density functional theory was performed within VASP simulation package. The exchange and correlation functions in the electron wave function were addressed by the Perdew-Burke-Ernzerhof (PBE) of generalized gradient approximation (GGA). The DFT-D3 functional was applied to describe dispersion relationships. All the systems were fully relaxed with an energy convergence $< 10^{-5} \text{ eV}$. To get optimized structures, total Hellmann-Feynman forces were reduced to 0.01 eV \AA^{-1} . The energy alteration of each step was reduced to 10^{-5} eV and the maximum displacement of atoms between each iteration step was $< 0.001 \text{ \AA}$. Cut-off energy of 500 eV was set for the plane wave expansion. The k -mesh was set by $8 \times 8 \times 8$ centered at the G point of Brillouin zone (BZ).

Statistical Analysis: Statistical analysis was performed using Origin 2022 (Origin Lab Corporation). Six independent Sb_2Se_3 MB-based PDs were fabricated for statistical analysis of the polarization sensitivity properties. Twenty Sb_2Se_3 MBs were randomly used for the size distribution measurement.

Supporting Information

Supporting Information is available from the Wiley Online Library or from the author.

Acknowledgements

This study was supported by the National Natural Science Foundation of China (Grant Nos. 11974182 and 11874220), the Fundamental Research Funds for the Central Universities (NO. NC2022008), and Funding for Outstanding Doctoral Dissertation in NUAA (BCXJ22-14).

Conflict of Interest

The authors declare no conflict of interest.

Data Availability Statement

The data that support the findings of this study are available in the supplementary material of this article.

Keywords

anisotropic properties, double-faced photodetection, near-infrared, polarization detection, perpendicular reversal

Received: July 6, 2022

Revised: August 1, 2022

Published online:

- [1] Y. Ping, H. Long, H. Liu, C. Chen, N. Zhang, H. Jing, J. Lu, Y. Zhao, Z. Yang, W. Li, F. Ma, X. S. Fang, Z. Wei, H. Xu, *Adv. Funct. Mater.* **2022**, *32*, 2111673.
- [2] Y. Li, Z. F. Shi, L. T. Wang, Y. Q. Liang, D. Wu, X. J. Li, Y. Zhang, C. X. Shan, X. S. Fang, *Mater. Horiz.* **2020**, *7*, 1613.
- [3] J. Bullock, M. Amani, J. Cho, Y. Z. Chen, G. H. Ahn, V. Adinolfi, V. R. Shrestha, Y. Gao, K. B. Crozier, Y. L. Chueh, A. Javey, *Nat. Photon.* **2018**, *12*, 601.
- [4] Z. L. Li, Z. Q. Li, C. L. Zuo, X. S. Fang, *Adv. Mater.* **2022**, *34*, 2109083.
- [5] E. Zhang, P. Wang, Z. Li, H. Wang, C. Song, C. Huang, Z. G. Chen, L. Yang, K. Zhang, S. Lu, W. Wang, S. Liu, H. Fang, X. Zhou, H. Yan, J. Zou, X. Wan, P. Zhou, W. Hu, F. Xiu, *ACS Nano* **2016**, *10*, 8067.
- [6] S. Zhang, H. Wang, M. M. Kirchner, J. Liu, H. Luo, Y. Ren, C. Yuan, H. T. Hattori, A. E. Miroshnichenko, W. Lei, *Adv. Mater. Interfaces* **2022**, *9*, 2200448.
- [7] G. Cao, H. Zhang, G. Chen, X. Li, *ACS Photon.* **2021**, *8*, 2459.
- [8] R. Chai, Y. Chen, M. Zhong, H. Yang, F. Yan, M. Peng, Y. Sun, K. Wang, Z. Wei, W. Hu, Q. Liu, Z. Lou, G. Shen, *J. Mater. Chem. C* **2020**, *8*, 6388.
- [9] J. Wang, C. Jiang, W. Li, X. Xiao, *Adv. Opt. Mater.* **2022**, 2102436.
- [10] H. Yuan, X. Liu, F. Afshinmanesh, W. Li, G. Xu, J. Sun, B. Lian, A. G. Curto, G. Ye, Y. Hikita, Z. Shen, S. C. Zhang, X. Chen, M. Brongersma, H. Y. Hwang, Y. Cui, *Nat. Nanotechnol.* **2015**, *10*, 707.
- [11] X. Zhou, X. Hu, S. Zhou, Q. Zhang, H. Li, T. Zhai, *Adv. Funct. Mater.* **2017**, *27*, 1703858.
- [12] X. Li, X. Dai, D. Tang, X. Wang, J. Hong, C. Chen, Y. Yang, J. Lu, J. Zhu, Z. Lei, K. Suenaga, F. Ding, H. Xu, *Adv. Funct. Mater.* **2021**, *31*, 2102138.
- [13] L. Pi, C. Hu, W. Shen, L. Li, P. Luo, X. Hu, P. Chen, D. Li, Z. Li, X. Zhou, T. Zhai, *Adv. Funct. Mater.* **2021**, *31*, 2006774.
- [14] J. Wang, M. S. Gudiksen, X. Duan, Y. Cui, C. M. Lieber, *Science* **2001**, *293*, 1455.
- [15] Y. Zhou, J. Luo, Y. Zhao, C. Ge, C. Wang, L. Gao, C. Zhang, M. Hu, G. Niu, J. Tang, *Adv. Opt. Mater.* **2018**, *6*, 1800679.
- [16] S. Liu, W. Xiao, M. Zhong, L. Pan, X. Wang, H. X. Deng, J. Liu, J. Li, Z. Wei, *Nanotechnology* **2018**, *29*, 184002.
- [17] Z. Ma, S. Chai, Q. Feng, L. Li, X. Li, L. Huang, D. Liu, J. Sun, R. Jiang, T. Zhai, H. Xu, *Small* **2019**, *15*, 1805307.
- [18] J. Wang, S. U. Rehman, Y. Xu, B. Zuo, H. Cheng, L. Guo, B. Zou, X. Zhang, C. Li, *Sol. Energy* **2022**, *233*, 213.
- [19] Y. Liu, C. Liu, K. Shen, P. Sun, W. Li, C. Zhao, Z. Ji, Y. Mai, W. Mai, *ACS Nano* **2022**, *16*, 5820.
- [20] Y. Xin, J. Jiang, Y. Lu, H. Liang, Y. J. Zeng, Z. Ye, *Adv. Mater. Interfaces* **2021**, *8*, 2100058.
- [21] R. Tang, S. Chen, Z. H. Zheng, Z. H. Su, J. T. Luo, P. Fan, X. H. Zhang, J. Tang, G. X. Liang, *Adv. Mater.* **2022**, *34*, 2109078.
- [22] Z. Li, X. Liang, G. Li, H. Liu, H. Zhang, J. Guo, J. Chen, K. Shen, X. San, W. Yu, R. E. Schropp, Y. Mai, *Nat. Commun.* **2019**, *10*, 125.
- [23] N. Tideswell, F. Kruse, J. McCullough, *Acta Crystallogr.* **1957**, *10*, 99.
- [24] M. Zhao, J. Su, Y. Zhao, P. Luo, F. Wang, W. Han, Y. Li, X. Zu, L. Qiao, T. Zhai, *Adv. Funct. Mater.* **2020**, *30*, 1909849.
- [25] L. Yu, B. Wang, H. Han, C. Dai, W. Liu, Y. Wang, *J. Lumin.* **2022**, *244*, 118704.
- [26] D. Wang, D. Yu, M. Mo, X. Liu, Y. Qian, *J. Cryst. Growth* **2003**, *253*, 445.
- [27] M. Chen, L. Gao, *Mater. Res. Bull.* **2005**, *40*, 1120.
- [28] N. Fleck, T. D. Hobson, C. N. Savory, J. Buckeridge, T. D. Veal, M. R. Correia, D. O. Scanlon, K. Durose, F. Jäckel, *J. Mater. Chem. A* **2020**, *8*, 8337.
- [29] J. Black, E. Conwell, L. Seigle, C. Spencer, *J. Phys. Chem. Solids* **1957**, *2*, 240.
- [30] F. Kosek, J. Tulka, L. Stourac, *Czech. J. Phys.* **1978**, *28*, 325.
- [31] C. Zhao, X. Cao, X. Lan, *Mater. Lett.* **2007**, *61*, 5083.
- [32] H. Song, T. Li, J. Zhang, Y. Zhou, J. Luo, C. Chen, B. Yang, C. Ge, Y. Wu, J. Tang, *Adv. Mater.* **2017**, *29*, 1700441.
- [33] H. Deng, S. Chen, M. Ishaq, Y. Cheng, Q. Sun, X. Lin, Q. Zheng, C. Zhang, S. Cheng, *Sol. RRL* **2022**, *6*, 2101017.
- [34] K. Li, C. Chen, S. Lu, C. Wang, S. Wang, Y. Lu, J. Tang, *Adv. Mater.* **2019**, *31*, 1903914.
- [35] Y. Zhou, L. Wang, S. Chen, S. Qin, X. Liu, J. Chen, D. J. Xue, M. Luo, Y. Cao, Y. Cheng, E. H. Sargent, J. Tang, *Nat. Photon.* **2015**, *9*, 409.
- [36] W. Yang, J. Ahn, Y. Oh, J. Tan, H. Lee, J. Park, H. C. Kwon, J. Kim, W. Jo, J. Kim, J. Moon, *Adv. Energy Mater.* **2018**, *8*, 1702888.
- [37] A. Shongalova, M. Correia, B. Vermang, J. Cunha, P. Salomé, P. Fernandes, *MRS Commun.* **2018**, *8*, 865.
- [38] P. Vidal-Fuentes, M. Guc, X. Alcobe, T. Jawhari, M. Placidi, A. Pérez-Rodríguez, E. Saucedo, V. I. Roca, *2D Mater.* **2019**, *6*, 045054.
- [39] Q. Zhao, F. Gao, H. Chen, W. Gao, M. Xia, Y. Pan, H. Shi, S. Su, X. S. Fang, J. Li, *Mater. Horiz.* **2021**, *8*, 3113.
- [40] H. Zhang, Y. Li, X. Hu, J. Xu, L. Chen, G. Li, S. Yin, J. Chen, C. Tan, X. Kan, L. Li, *Appl. Phys. Lett.* **2021**, *119*, 171102.
- [41] R. Loudon, *Adv. Phys.* **1964**, *13*, 423.
- [42] P. Wan, M. Jiang, T. Xu, Y. Liu, X. S. Fang, C. Kan, *Adv. Opt. Mater.* **2022**, *10*, 2101851.
- [43] P. Wan, M. Jiang, T. Xu, Y. Liu, C. Kan, *J. Mater. Sci. Technol.* **2021**, *93*, 33.
- [44] X. Wen, Z. Lu, L. Valdman, G. C. Wang, M. Washington, T. M. Lu, *ACS Appl. Mater. Interfaces* **2020**, *12*, 35222.
- [45] S. Chen, X. Qiao, F. Wang, Q. Luo, X. Zhang, X. Wan, Y. Xu, X. Fan, *Nanoscale* **2016**, *8*, 2277.
- [46] F. Cao, Z. Pan, X. Jia, *J. Appl. Phys.* **2021**, *129*, 204503.
- [47] W. D. Song, J. Chen, Z. Li, X. S. Fang, *Adv. Mater.* **2021**, *33*, 2101059.
- [48] X. Liu, J. Chen, M. Luo, M. Leng, Z. Xia, Y. Zhou, S. Qin, D. J. Xue, L. Lv, H. Huang, D. Niu, J. Tang, *ACS Appl. Mater. Interfaces* **2014**, *6*, 10687.
- [49] D. A. Neamen, *Semiconductor Physics and Devices: Basic Principles*, 3rd ed., Irwin Inc, Boston, MA **1992**.
- [50] J. X. Chen, X. Y. Liu, Z. Q. Li, F. Cao, X. Lu, X. S. Fang, *Adv. Funct. Mater.* **2022**, *32*, 2201066.
- [51] C. Chen, D. C. Bobela, Y. Yang, S. Lu, K. Zeng, C. Ge, B. Yang, L. Gao, Y. Zhao, M. C. Beard, J. Tang, *Front. Optoelectron.* **2017**, *10*, 18.
- [52] L. Gao, K. Zeng, J. Guo, C. Ge, J. Du, Y. Zhao, C. Chen, H. Deng, Y. He, H. Song, G. Niu, J. Tang, *Nano Lett.* **2016**, *16*, 7446.
- [53] J. Shaffer, B. Van Pelt, C. Wood, J. Freeouf, K. Murase, J. Osmun, *Phys. Status Solidi B* **1972**, *54*, 511.